

LA-UR-16-27965

Approved for public release; distribution is unlimited.

Title: Discrete Fracture Network Modeling and Simulation of Subsurface Transport for the Topopah Springs and Lava Flow Aquifers at Pahute Mesa, FY 15 Progress Report

Author(s): Makedonska, Natalia
Kwicklis, Edward Michael
Birdsell, Kay Hanson
Harrod, Jeremy Ashcraft
Karra, Satish

Intended for: Report

Issued: 2016-10-18

Disclaimer:

Los Alamos National Laboratory, an affirmative action/equal opportunity employer, is operated by the Los Alamos National Security, LLC for the National Nuclear Security Administration of the U.S. Department of Energy under contract DE-AC52-06NA25396. By approving this article, the publisher recognizes that the U.S. Government retains nonexclusive, royalty-free license to publish or reproduce the published form of this contribution, or to allow others to do so, for U.S. Government purposes. Los Alamos National Laboratory requests that the publisher identify this article as work performed under the auspices of the U.S. Department of Energy. Los Alamos National Laboratory strongly supports academic freedom and a researcher's right to publish; as an institution, however, the Laboratory does not endorse the viewpoint of a publication or guarantee its technical correctness.

**Discrete Fracture Network Modeling and Simulation of Subsurface Transport for the
Topopah Springs and Lava Flow Aquifers at Pahute Mesa**

FY 15 Progress Report

Nataliia Makedonska, Edward Kwicklis, Kay Birdsell, Jeremy Harrod, and Satish Karra

Los Alamos National Laboratory

March 2016

This progress report for fiscal year 2015 (FY15) describes the development of discrete fracture network (DFN) models for Pahute Mesa. DFN models will be used to upscale parameters for simulations of subsurface flow and transport in fractured media in Pahute Mesa. The research focuses on modeling of groundwater flow and contaminant transport using DFNs generated according to fracture characteristics observed in the Topopah Spring Aquifer (TSA) and the Lava Flow Aquifer (LFA). This work will improve the representation of radionuclide transport processes in large-scale, regulatory-focused models with a view to reduce pessimistic bounding approximations and provide more realistic contaminant boundary calculations that can be used to describe the future extent of contaminated groundwater. Our goal is to refine a modeling approach that can translate parameters to larger-scale models that account for local-scale flow and transport processes, which tend to attenuate migration.

The TSA and LFA at Pahute Mesa are highly fractured heterogeneous aquifers for which detailed modeling of radionuclide transport on a small scale with subsequent upscaling is appropriate. For this study, we used *dfnWorks* software that was recently developed at LANL. *dfnWorks* is used to simulate fracture flow and advective contaminant transport through fractures, where groundwater flow and radionuclide migration may be rapid. Transport modeling provides the pathlines of contaminant particles. These results may then become input to *MARFA* or *PLUMECALC* software to evaluate the impacts of adsorption and matrix diffusion on transport. Using this approach, we plan to incorporate local advective velocities and mass exchange between fractures and matrix, combined with retention processes (diffusion, sorption) in the matrix, which may strongly influence transport at the time and spatial scales relevant for Pahute Mesa. Moreover, we plan to use the process to define upscaled equivalent parameters and estimate transport characteristics at scales appropriate for contaminant boundary calculations while accounting for local-scale flow and transport processes that tend to attenuate migration.

In this progress report, two simple discrete fracture networks are presented as verification examples, where numerical results are compared with analytical solutions. We then show preliminary results of fracture network modeling of complex networks for the TSA and LFA of Pahute Mesa.

1. Introduction

Discrete fracture network (DFN) modeling is being used to study contaminant transport in aquifers for the Underground Test Area (UGTA) activity at the Nevada National Security Site. The recently developed computational suite, *dfnWorks* [Hyman et al., 2015a], is used to model steady-state, fully-saturated flow, and particle movement through a DFN. In the model, planar objects randomly placed in a three-dimensional domain intersect each other to represent fracture networks. Fractures are assigned their size, shape, location, orientation, and aperture. Fracture sizes and orientation are stochastically defined based on site-specific data. The generation of fractures is performed via the FRAM algorithm, described in detail in [Hyman et al., 2014]; these fractures are subsequently used to generate a high-quality computational Delaunay triangulation mesh with LaGriT [LaGriT, 2013]. The control volume cells are formed based on Delaunay triangulations. The highly-parallel, multiphysics code, PFLOTRAN [Lichtner et al., 2015], is used as the control volume solver, to obtain the steady-state flow solution with applied pressure boundary conditions. The Lagrangian particle tracking model [Makedonska et al., 2015] is applied to simulate advective transport through three-dimensional DFNs. The workflow of *dfnWorks* is described in Section 2.

We refer the reader to [Hyman et al., 2015a] for further details and applications of *dfnWorks* software. This software was successfully verified and tested on a 1-km cube DFN that was generated according to the fractured rock characteristics of the proposed nuclear repository site in Forsmark, Sweden [SKB, 2011]. The effect of particle injection mode on transport properties in the large-scale DFN was studied in [Hyman et al., 2015b]. Moreover, we are able to model in-fracture variability of aperture and transmissivity in each individual fracture in a network of thousands of fractures.

For this study, *dfnWorks* software is used to model fracture networks observed at Pahute Mesa for the Topopah Spring Aquifer (TSA) and Lava Flow Aquifers (LFA). Fractures are generated according to fracture characteristics data provided by *Golder and Associates*, where parameters on distributions of fracture orientations and fracture sizes, network intensities P_{32} , and fracture conductive characteristics, such as aperture and transmissivity are included [Appendix L of NSTec, 2014; Tech. Mem, 2014].

In order to verify the workflow of our DFN analysis, we start with the generation of two simple DFNs and calculate the hydrologic properties of the individual fractures, obtain steady-state pressure solutions for the DFNs, and run particle tracking. The upscaled parameters, such as effective permeability, transport porosity, and volumetric porosity, are estimated. We show our results for the DFNs generated for the TSA and LFA fracture characteristics. The breakthrough curves of particles are calculated for transport in different directions of flow: west-east, south-north, and top-bottom to determine the anisotropy in the networks.

2. Computational Suite for Modeling Flow and Transport in 3-D Discrete Fracture Networks, *dfnWorks*

An overview of the entire *dfnWorks* workflow is illustrated in Figure 1 (corresponds to Fig. 2 in Hyman et al., 2015). The workflow has three principal pieces (dfnGen, dfnFlow, dfnTrans), which can be broken down into six primary aspects. The inputs for *dfnWorks* are fracture site characteristics that provide distributions of fracture orientations, radii, and spatial locations.

dfnGen: (1) fram [Hyman et al., 2014]— create DFN: using the fractured site characteristics, networks are constructed using the feature rejection algorithm for meshing. (2) LaGriT – mesh DFN: the LaGriT meshing toolbox is used to create a conforming Delaunay triangulation of the network.

dfnFlow: (3) convert mesh to PFLOTRAN input: control-volume information is formatted for PFLOTRAN. (4) Compute pressure solution: the steady-state pressure solution in the DFN is obtained using PFLOTRAN [Lichtner et al., 2015].

dfnTrans: (5) reconstruct local velocity field: Darcy fluxes obtained using dfnFlow are used to reconstruct the local velocity field, which is used for particle tracking on the DFN. (6) Lagrangian transport simulation: an extension of the walkabout method [Painter et al., 2012] is used to determine pathlines through the network and simulate transport. It is important to note that dfnTrans itself only solves for advective transport, but effects of longitudinal dispersion and matrix diffusion, sorption, and other retention processes are easily incorporated by post-processing particle trajectories [Painter et al., 2008]. In our work, we use the MARFA software [Painter et al., 2013] to include retention processes in transport modeling and update breakthrough curves to reflect those processes.

Communication between the different pieces of the *dfnWorks* workflow is carried out using files that allow for restarts between the different modules of the code. Various python scripts are used to format the output from one stage of the workflow into the required input format of the next stage. Coupling between the pieces of the workflow is fully automated and does not require user actions. One of the key features of *dfnWorks* is that it combines existing software, e.g., LaGriT and PFLOTRAN, in a novel workflow. The primary benefits of this choice are that the combined codes have already been optimized with respect to their efficiency, and that verification and validation have already been performed and documented [Hyman et al., 2015a].

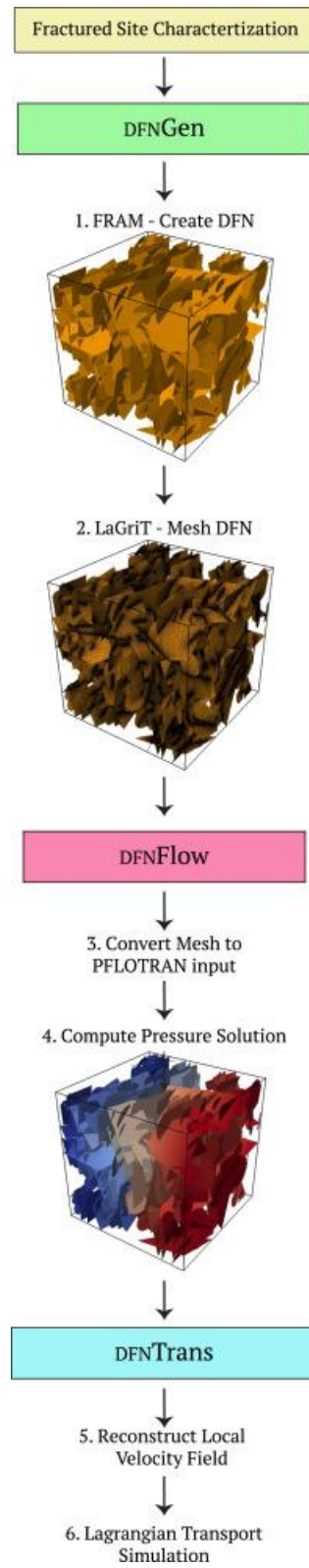


Figure 1. *dfnWorks* Workflow

3. Verification of the Workflow of the Contaminant Transport Modeling on Simple DFNs

There are two simple DFN models we consider for workflow verification.

- Verification Test #1: 10 identical, non-intersecting, horizontal fractures placed in a 3D domain.
- Verification Test #2: A combination of perpendicular horizontal and vertical fractures forms a fracture network in a 3D domain.

In each case, the effective permeability is calculated and compared to analytical results.

3.1 Verification Test #1: 10 Horizontal Fractures

The following simple fracture network (Figure 2) was chosen as a first verification test of the workflow used for contaminant transport modeling in DFNs:

- Domain size is 100 m x 100 m x 100 m.
- 10 horizontal fractures are equidistant from each other with 10-m spacing
- Fractures are oriented parallel to the xy plane and perpendicular to the z axis. The size of the horizontal fractures is 100 m x 100 m.

The conductive properties of the fractures are similar to those defined for Pahute Mesa [Appendix L of NSTec, 2014 (draft PM HFM Report)]. The fracture transmissivity is correlated to fracture length according to the following equation:

$$\text{Transmissivity} = 5 \times 10^{-8} L^{1.3681}, [\text{m}^2/\text{s}] \quad (1)$$

Fracture aperture is assumed to be directly correlated to fracture transmissivity using the following equation:

$$\text{Aperture} = 10 * \text{Transmissivity}^{0.5}, [\text{m}] \quad (2)$$

The above equations are given in Section 5.1.4 “Hydraulic Property Model Parametrization” in Appendix L of the PM HFM report [NSTec, 2014]. The cubic law for fracture transmissivity is not used in this study.

Using these equations, the conductive properties are the same in each fracture:

- $\text{Aperture}_{\text{horizontal}} = 0.0522 \text{ [m]}$
- $\text{Transmissivity}_{\text{horizontal}} = 2.724 \times 10^{-5} \text{ [m}^2/\text{s}]$

Hydraulic features such as aperture and transmissivity are attributes assigned to the vertices of the computational mesh generated for each fracture (Figure 2, right panel).

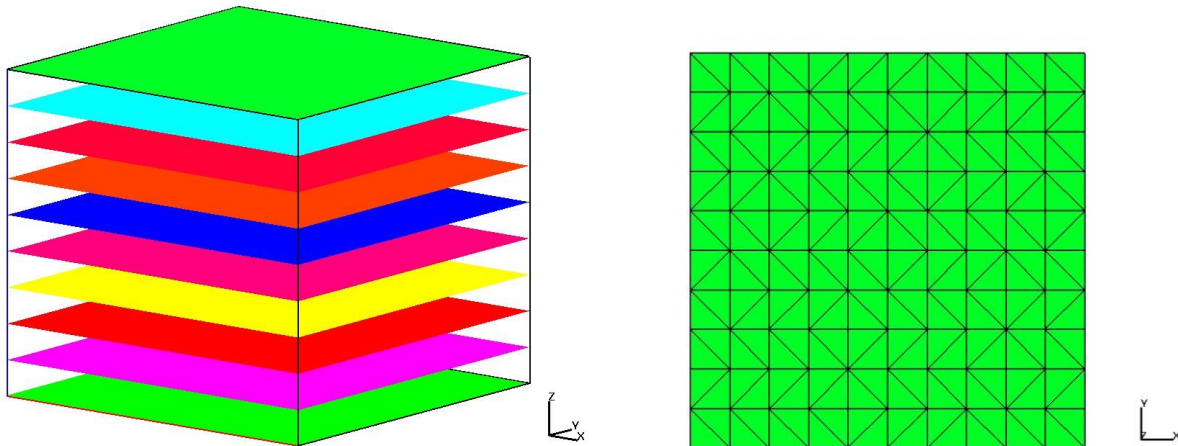


Figure 2. Left panel: 10 horizontal fractures (each shown by its own color) parallel to the xy -plane are used for the first verification test. Domain size is $100 \text{ m} \times 100 \text{ m} \times 100 \text{ m}$; there is a 10-m vertical spacing between fractures. Right panel shows Delaunay triangulations for the computational mesh of a single fracture.

Pressure boundary conditions are applied to the south ($+y$) and north ($-y$) boundaries of the domain. The boundary vertices of fractures located on the south face of the domain are given a higher pressure (1.01 MPa) and boundary vertices on the north side are assigned a lower pressure (1.0 MPa), which creates 10 kPa pressure gradient across each fracture. Then, the steady-state pressure solution for fully saturated flow is calculated by PFLOTRAN [Lichtner et al., 2015]. The obtained pressure solution is shown in Figure 3.

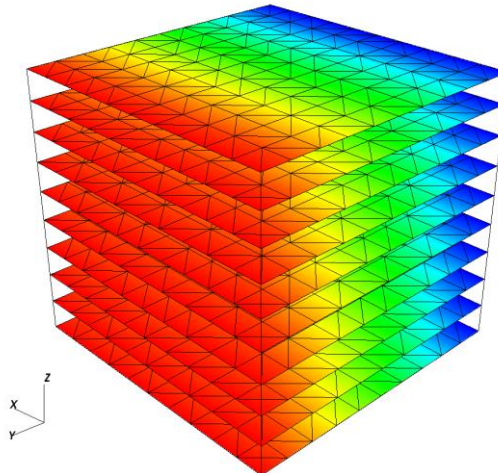


Figure 3. Pressure solution for fully saturated flow. Here higher pressure (red = 1.01 MPa) is applied to the $+y$ (south) side of the domain, and lower pressure (blue = 1 MPa) is applied to the $-y$ (north) side of the domain. The simulation assumes that flow goes from south to north. Black solid lines represent the computational mesh.

PFLOTRAN provides flow fluxes, q [m/s], on each face of every control volume cell (Voronoi polygon). Darcy velocity at each face can be found as q/ϕ_f , where ϕ_f is the internal fracture porosity. We consider two values of internal fracture porosity: $\phi_f=0.25$ and $\phi_f=1.0$. In the ideal case, we assume that the fractures are represented by two parallel plates, and the internal fracture porosity $\phi_f=1.0$. The porosity $\phi_f=0.25$ is used to represent internal heterogeneity in natural fractures, which can be caused by variable aperture or fracture fill within the fractures.

We use the Lagrangian method to simulate transport [Makedonska et al., 2015]. In order to model transport, the Darcy velocities are reconstructed on each vertex of the computational mesh from flow fluxes, q , given by flow solver on each face of the control-volume units. The numerically obtained Darcy velocities in a 3D DFN are vectors with three components: v_x , v_y , and v_z . In our example, the largest velocity component is v_y , since flow is along the y axis. v_x and v_z are essentially zero. Figure 4 shows particle trajectories for a simulation in which 20 particles are initially placed equidistantly on each fracture boundary and tracked from the in-flow (south) to the out-flow (north) boundary of the domain. The particles trajectories are straight across the domain as dictated by the velocity vectors. There is no dispersion in these calculations.

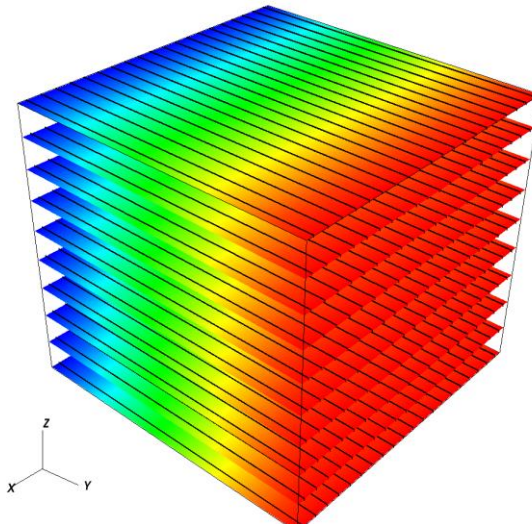


Figure 4. Twenty particle trajectories (black lines) for each of 10 horizontal fractures. Colors represent pressure, similar to those in Figure 3. Particles move from high to low pressure along the y axis.

Particle breakthrough for 5000 particles was calculated to determine travel times. The numerical travel times calculated are $t_{\text{numerical}}(\phi_f=0.25)=4.6972\text{e}6$ [s] and $t_{\text{numerical}}(\phi_f=1.0)=1.8788\text{e}7$ [s] for a fracture porosity of 0.25 and 1.0, respectively. In each case, all particles breakthrough at the downstream boundary at identical times because each fracture is assigned the same aperture and transmissivity, and longitudinal dispersivity is zero in this simple example.

These numerical results are compared to an analytical solution for this system:

1. Single fracture permeability, k [m^2], is defined from fracture transmissivity, as

$$k = \mu \frac{Ks}{\rho g}$$
, where Ks is a hydraulic conductivity, $Ks=\text{Transmissivity} / \text{Aperture} = 5.2184\text{e-}4[\text{m/s}]$;

$\mu = 8.9 \text{ e-4} [\text{Pa s}]$ is the water viscosity; g is a gravity acceleration, $g=9.8 [\text{m/s}^2]$; ρ is a water density, $\rho=1000 [\text{kg/m}^3]$. Therefore, permeability in our case is $k=4.7393e-11 [\text{m}^2]$.

2. In order to calculate inflow flux, $q [\text{m/s}]$, the Darcy Law is used:

$$q = \frac{k \Delta p}{\mu L}$$
, where Δp is a pressure gradient, $\Delta p=10e4 [\text{Pa}]$ (section 3.2.1 shows how the pressure gradient is calculated); $L = 100 [\text{m}]$ is a length of the domain along the flow direction. Flow flux, $q [\text{m/s}]$, in each single horizontal fracture is $q=5.3249e-6 [\text{m/s}]$.

3. Particles velocity is defined as q/ϕ_f , where ϕ_f is the internal fracture porosity. We consider two values of internal fracture porosity: $\phi_f=0.25$ and $\phi_f=1.0$. As a result, velocity $v(\phi_f=0.25)=2.130e-5[\text{m/s}]$, and $v(\phi_f=1.0)= 5.3249e-6 [\text{m/s}]$.
4. Travel time of particles is L/v , where $L =100 [\text{m}]$ is the fracture length in the direction of flow. Travel time $t_{\text{analytical}}(\phi_f=0.25)=4.6948e6[\text{s}]$, and $t_{\text{analytical}}(\phi_f=1.0)=1.878e7[\text{s}]$.

Therefore, the numerical and analytical results for the Darcy velocities and travel times for flow and transport through horizontal fractures is verified for Test #1.

3.2 Verification Test #2: 10 Horizontal Fractures Combined with 9 Vertical Fractures

In the second verification test, we increase the geometric complexity of the first test, adding 9 vertical fractures to the 10 horizontal fractures considered in the previous example (Section 3.1). The horizontal and vertical fractures intersect each other and form a simple 3D fracture network. Now, all six boundaries of the simulation domain are connected through the network, which makes it possible to model transport in multiple directions by modifying the boundary conditions. The DFN is shown in Figure 5, and its characteristics are listed below:

- Domain size is 100 m x 100 m x 100 m.
- 10 horizontal fractures are equidistant from each other, oriented parallel to the xy plane and perpendicular to the z axis. The size of the horizontal fractures is 200 m x 200 m.
- 9 vertical fractures are orthogonal to the horizontal fractures. They are oriented perpendicular to the xy plane. The size of the vertical fractures is 80 m x 120 m. We note that these fractures do not extend across the entire domain, which adds to the anisotropic nature of this example.
- Fracture sizes for both sets exceed the domain size and are truncated. The truncation procedure is common in the *dfnWorks* fracture-generation process. For the horizontal fractures, the domain size is exceeded in both directions, and the fractures extend the entire 100-m length of the domain. For the vertical fractures, the domain size is exceeded in the z -direction, and the fractures span the length of the domain; however, in the y -direction, the fractures are 80-m long and stop 10-m short of the domain edges on either side (Figure 5). Despite being truncated, the fracture hydrologic properties are calculated according to the initial fracture sizes causing the horizontal and vertical fracture sets to have different properties.

Figure 5 shows the DFN, where each fracture is shown by its own color.

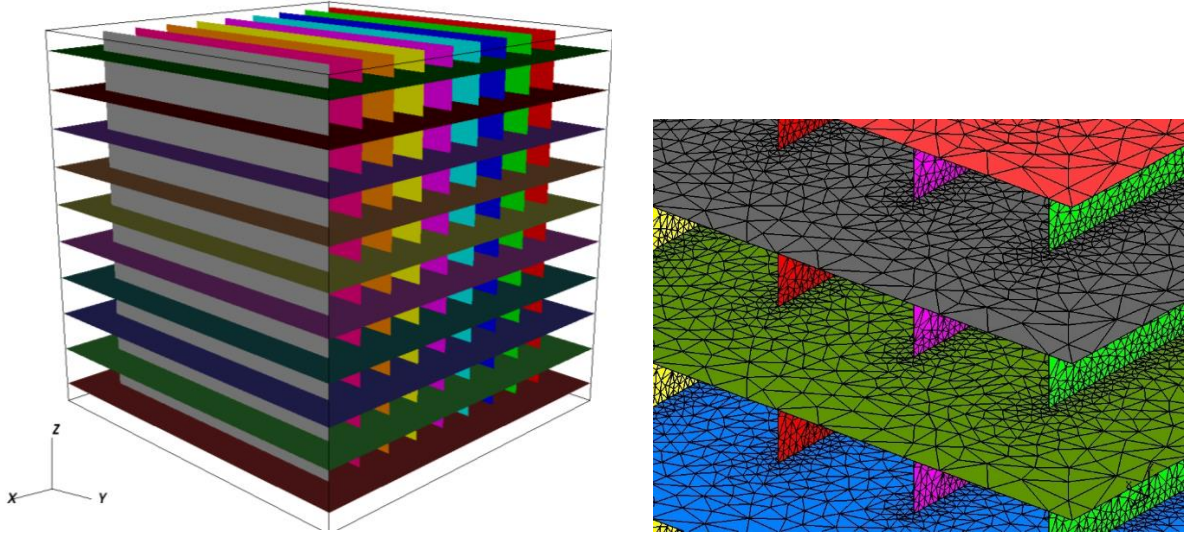


Figure 5. Left panel: 10 horizontal and 9 vertical fractures used in verification test #2. The fractures are orthogonal to each other and have equidistant spacing in the three-dimensional domain. The domain size is 100 m x 100 m x 100 m. The right panel shows an enlargement of the Delaunay triangulations in the mesh near the intersection of the vertical and horizontal fractures.

Assuming that the fracture horizontal and vertical half-lengths are 100 m and 40 m, respectively, the calculated aperture and transmissivity values based on Equations (1) and (2) are:

- Aperture_{horizontal}=0.0522 [m]
- Aperture_{vertical} = 0.0279 [m]
- Transmissivity_{horizontal} = 2.724×10^{-5} [m²/s]
- Transmissivity_{vertical} = 7.776×10^{-6} [m²/s]

The lengths 100 m and 40 m are chosen so that the difference in aperture and transmissivity of the vertical and horizontal fractures is significant. These differences have an important influence on the calculated effective permeability and transport parameters in the vertical and horizontal directions of flow.

Figure 6 (left panel) shows the calculated transmissivity distribution within the fracture network. In the DFN model, fractures are modeled as two-dimensional polygons, and features such as aperture and transmissivity are attributes assigned to the vertices of the computational mesh generated for each fracture.

3.2.1 Steady-State Flow Solution

The next step is to apply pressure boundary conditions to obtain steady-state flow solutions for fully saturated flow. First, the pressure gradient is calculated.

Given a hydraulic gradient $i=0.01$ [m/m] = $(h_2 - h_1)/L$, where L is the length of the domain (L=100 m), and $h = P/\rho g$ [m], ρ is water density [kg/m³], g is an acceleration due to gravity [10 m/s²], the pressure gradient can be calculated from

$$i = \frac{(P_2 - P_1)/\rho g}{L} \quad \rightarrow \quad P_2 - P_1 = i \rho g L \quad (3)$$

In our example, $L = 100$ m, and the calculated pressure difference is 10 kPa. Figure 7, right panel, shows an example of the calculated steady-state pressure solution, where pressure boundary conditions are applied to the north (low pressure) and south (high pressure) boundaries of the domain, assuming flow from south to north. No-flow boundary conditions are applied along the other four sides of the simulation domain. The pressure solution is simulated with PFLOTRAN [Lichtner et al., 2015]. With this orientation of flow, the pressure gradient is applied to both the horizontal and vertical fracture sets because all fracture sets extend to the south and north boundaries.

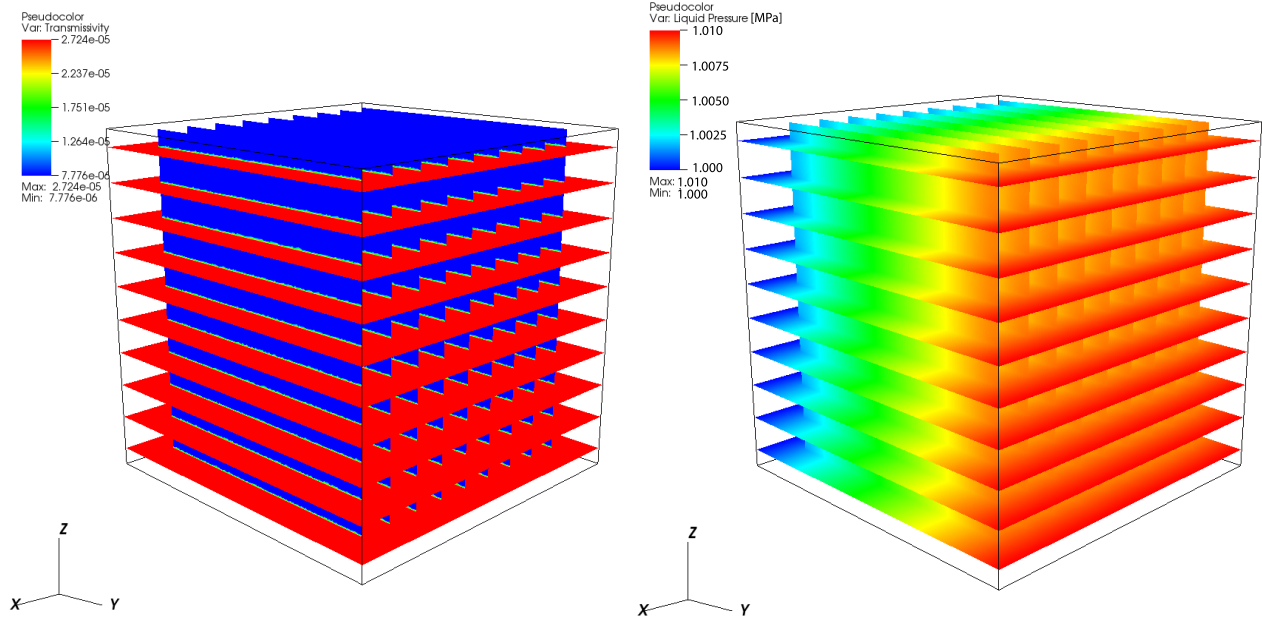


Figure 6. The left panel shows the transmissivity (Eq. 1) distribution along the fracture network for verification test #2. The horizontal fractures have higher transmissivity than the vertical fractures because the horizontal fracture length is larger than the vertical fracture length. The right panel shows an example of the simulated pressure solution for fully saturated flow. Here, high pressure (red) is applied to the $+y$ (south) side of the domain, and low pressure (blue) is applied to the $-y$ (north) side of the domain; flow is from south to north.

3.2.2 Particle Tracking in Discrete Fracture Networks

Particle tracking simulations are performed with *dfnTrans*, the transport model within the *dfnWorks* software. The following steps are included in the modeling process:

- Darcy velocity reconstruction from flow fluxes for each node of the computational mesh. Here we test two values of internal fracture porosity, $\phi_f=0.25$ and $\phi_f=1.0$, in velocity calculations;
- Splitting of flow velocities on the vertices at fracture intersection lines to explicitly represent the individual flow directions present at each fracture intersection;
- Barycentric interpolation to identify instantaneous velocities of a particle at any fracture location in the DFN. This interpolation allows accurate calculation of the particle velocity when the particle is not located at a mesh node (i.e., the particle moves at a resolution that is finer than the mesh, [Coxeter, 1969]);

- Application of a probabilistic approach, based on flow fluxes, at fracture intersections to determine the direction of the next particle movement. A detailed explanation of the particle-tracking approach can be found in [Makedonska et al., 2015].

In the current example, 500 particles are placed initially on each fracture edge that crosses the in-flow boundary, which results in 5,000 particles travelling through the DFN in the horizontal direction and 4,500 in the vertical direction. Particles are seeded equidistant from each other on the in-flow boundary, then they are followed to the out-flow boundary using a Predictor-Corrector method implemented in the particle tracking code, *dfnTrans*. Figure 7 shows breakthrough curves (BTCs) for particles moving in each direction of the domain. We use cumulative distribution functions (CDF) to plot the BTCs.

We can analytically estimate travel times in both the horizontal and vertical directions of flow similar to previous example of horizontal fractures only (Verification Test #1). For this analytical estimate, we assume only horizontal or only vertical fractures are present in the system. The results for the analytical calculations are given in Table 1. The modeled fracture networks are more complicated than these analytical estimates, but the analytical estimates help to judge that the DFN solutions are in the correct range.

Table 1. Analytical estimates of transport travel times for single horizontal and vertical fractures in DFN Test #2

	Horizontal direction West-East, North-South	Vertical direction Top-Bottom
Fracture aperture, [m]	0.0522	0.0279
Fracture transmissivity, [m ² /s]	2.724e-5	7.776e-6
Hydraulic conductivity, K _s , [m/s], K _s =transmissivity/aperture	5.218e-4	2.787e-4
Fracture permeability, k, [m ²], k = $\mu \frac{K_s}{\rho g}$	4.739e-11	2.531e-11
Flow flux, q, [m/s], q = $\frac{k \Delta p}{\mu L}$	5.325e-6	2.844e-6
Transport velocity ($\phi_f=0.25$) [m/s], v=q/φ	2.130e-5	1.138e-5
Transport velocity ($\phi_f=1.0$) [m/s], v=q/φ	5.325e-6	2.844e-6
Travel time, [s], L/v($\phi_f=0.25$)	4.706e6	8.790e6
Travel time, [s], L/v($\phi_f=1.0$)	1.882e7	3.517e7

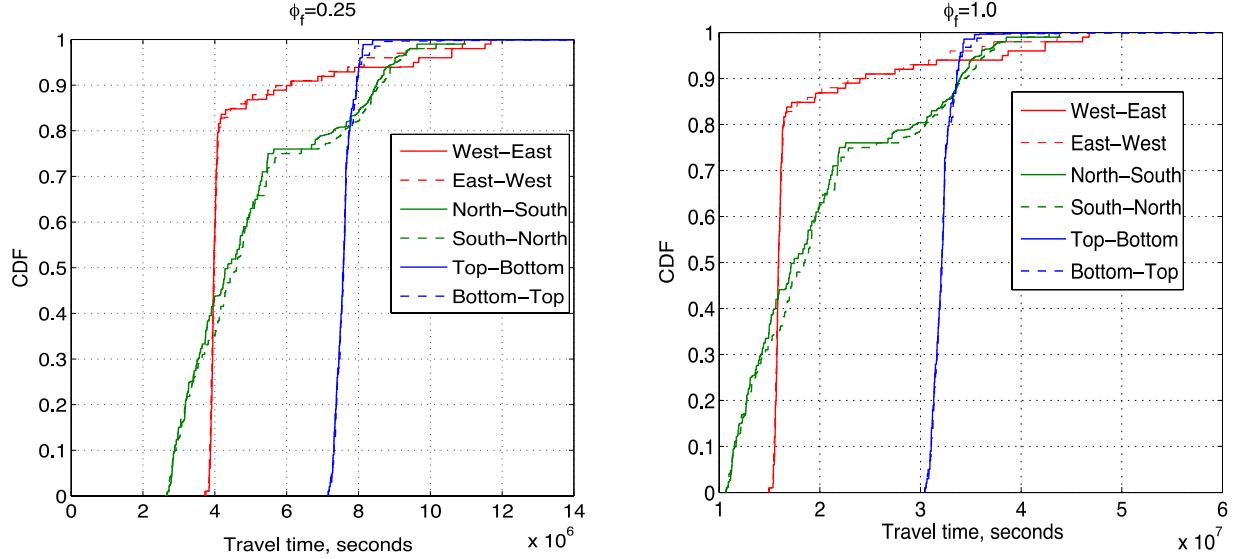


Figure 7. Breakthrough curves (CDF function) are plotted for 5000 particles traveling in each direction of flow across the domain for verification test #2. Left panel corresponds to results of particles travel time with internal fracture porosity $\phi_f=0.25$. Right panel shows BTC for internal fracture porosity $\phi_f=1.0$.

By analyzing the BTCs (Figure 7), we can see that most of the particles have mean travel times close to those estimated analytically; however, there are many particles that show longer travel times due to dispersion caused by particles migrating into different fractures than the ones in which they were originally introduced. For a given directional pair (e.g., North-South (NS) vs. South-North (SN) flow), similar behavior is observed in the two directions, as expected because the network is symmetric. More than 80% of the particles preferentially travel straight from the in-flow to the out-flow boundaries along the horizontal fractures as indicated by the changes in slope of the CDFs at 0.73 for the NS-SN CDFs and at 0.82 for the WE-EW CDFs. The remaining particles move at least part of the transport distance through vertical fractures and show longer travel times. The higher horizontal than vertical fracture transmissivity leads to faster breakthrough for the horizontal flow cases than for the vertical flow cases.

The greatest dispersion is observed along the NS-SN directions (Figure 7), for which particle trajectories are shown in Figure 8. This is explained by the orientation of the vertical fractures: vertical fractures are oriented along the flow direction and experience the pressure gradient in the same way as the horizontal fractures, which allows for particle transport along the vertical fractures as well. It is clearly observed that particles travel through both the horizontal and vertical fractures, although the predominant trajectories are horizontal. In this direction, the vertical fractures do not extend across the full length of the domain. Therefore, the particles that do migrate into the vertical fractures must find their way back to a horizontal fracture to exit at the northern boundary. The variable amounts of time particles spend in the low transmissivity vertical fractures results in hydrodynamic dispersion, which contributes to longer tails on the BTCs in the NS-SN directions compared with the case with only horizontal fractures. The earlier particle breakthrough in the NS-SN directions for this network compared with the case involving only horizontal fractures occurs because velocities in horizontal fractures are higher near their intersection with the vertical

fractures. Particles that travel close to, but do not enter the vertical fractures, break through earlier than particles traveling either part of the way in the vertical fractures or in the horizontal fractures midway between neighboring vertical fractures. For EW-WE flow, the pressure gradient does not align with the vertical fracture set in the same way, the particles stay predominantly in the horizontal fractures, and the BTCs indicate less dispersion. However, even for EW-WE flow, about 16 percent of the particles spend at least some portion of the time in the vertical fractures, as evidenced by their delayed breakthrough.

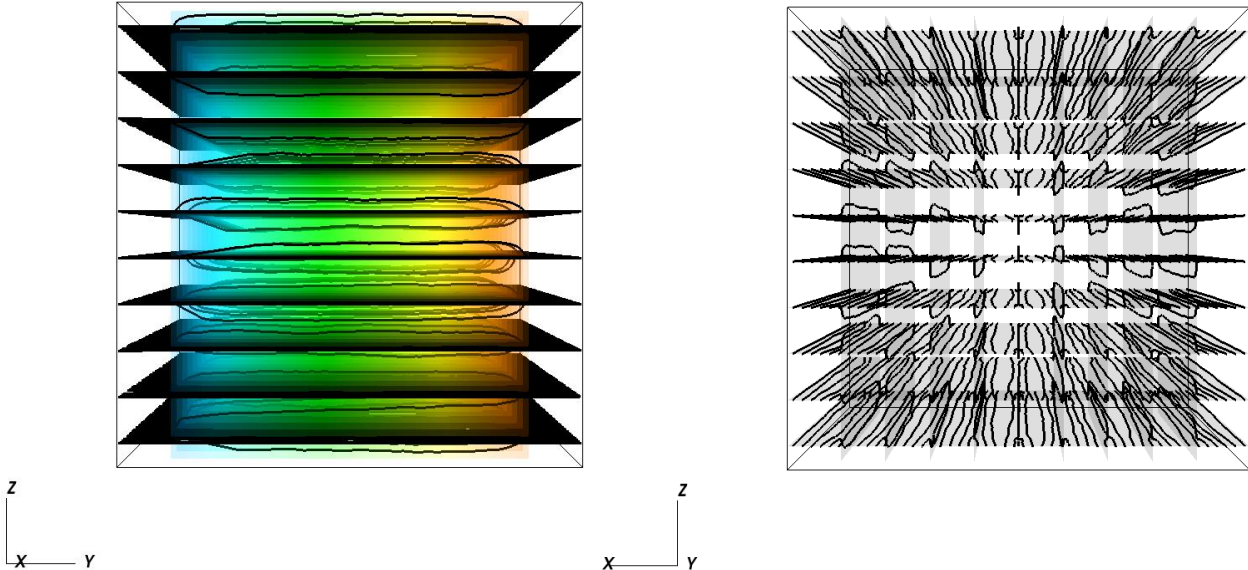


Figure 8. Two points of view are shown for particle trajectories, where particles are moving from south to north (from $+y$ to $-y$ sides), for verification test #2. The left panel shows trajectories along the y direction projected onto a y - z plane; the right panel shows the same trajectories projected onto a x - z plane point of view.

For the top-bottom and bottom-top flow directions, nearly all the particles show similar travel times through the domain. Trajectories of particles moving in vertical directions are shown in Figure 9. Here, very little transport into the horizontal fractures occurs because the gradient is aligned only along the vertical fractures and does not promote transport into the horizontal fractures, where the pressure has a single value along a given horizontal fracture. This yields a BTC with almost no dispersion (Figure 7).

Verification Test#2 shows that fracture orientations, their intersections, their conductive properties, the complex topology, and the structure of the fracture networks have a significant effect on particle trajectories, transport dispersion, and on transport travel times. Even this simple case illustrates the complex nature of particle transport through a DFN.

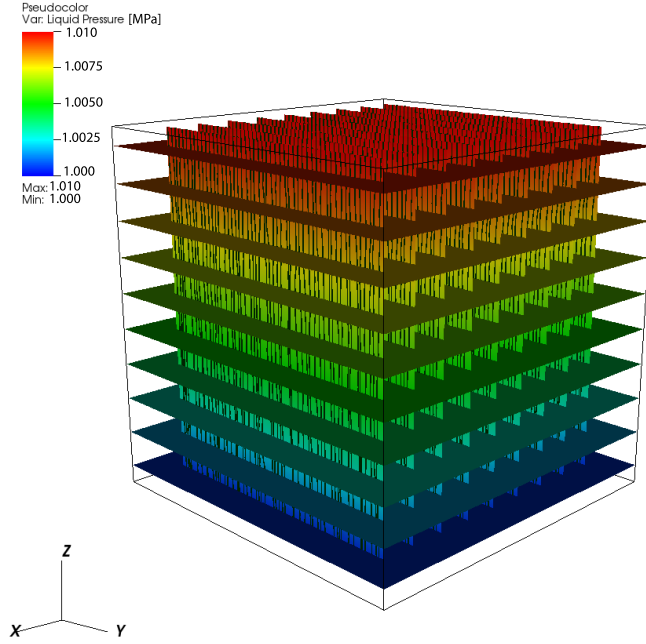


Figure 9. Pressure solution (color pattern) and the particle trajectories (black lines) for verification test #2 with flow from top to bottom, along the z (vertical) direction.

3.3 Upscaled Parameters Calculated for Verification Test #2

In this section, the following upscaled parameters are calculated: effective permeability, volumetric porosity and transport porosity.

- Effective permeability is calculated using Darcy's Law. Effective permeability is derived as a function of the Darcy flux.
- Volumetric porosity is computed using fracture sizes and their apertures. Volumetric porosity depends on the fracture geometry and the relationship between aperture and fracture size, such as Eq. 2.
- Transport porosity is a function of the particle travel time, volumetric porosity and internal fracture porosity.

In order to estimate the **effective bulk permeability**, k , of the entire domain, we use Darcy's Law:

$$Q = \frac{-kA}{\mu} \frac{(P_2 - P_1)}{L}, \quad (4)$$

where

$Q = [\text{m}^3/\text{s}]$ is a volumetric Darcy flux in and out of the model domain;

$\mu = 8.9 \cdot 10^{-4} [\text{Pa s}]$ is the water viscosity;

$L = 100 [\text{m}]$ is a length of the domain along the flow direction;

$A_h = 100 \text{ m} \times 100 \text{ m} = 10^4 \text{ m}^2$ is the total area of the in-flow boundary in the horizontal direction;

$A_v = 100 \text{ m} \times 100 \text{ m} = 10^4 \text{ m}^2$ is the total area of the in-flow boundary in the vertical direction;

$\Delta P = 10 \text{ [kPa]} = 10000 \text{ [Pa]}$ is the pressure gradient, defined by Eq. 3.

The input Darcy Flux per unit area, $q[\text{m/s}]$, is calculated by dividing the input volumetric Darcy flux, derived from Eq. 4, by the inflow area A :

$$q = \frac{Q}{A} = \frac{-k}{\mu} \frac{(P_2 - P_1)}{L} \quad (5)$$

Volumetric Darcy flux (Eq. 4) along a boundary is calculated as a sum of the input fluxes defined by the flow solver, PFLOTRAN, on fracture edges along the in-flow boundary:

$$\sum_{i=1}^N q_i a_i = Q, \quad (6)$$

where N is the number of computational cells of fractures on the in-flow boundary, q_i is an input flux defined for cell i , and a_i is the area of the cell face i on the in-flow boundary. The area of the cell face, a_i , is defined as the length of the 2d cell edge times the fracture aperture calculated by Eq.2 (aperture as a function of fracture length). Substituting Eq. 4 and Eq. 6 yields:

$$\sum_{i=1}^N q_i a_i = Q = \frac{-kA}{\mu} \frac{(P_2 - P_1)}{L} \quad (7)$$

From (7) effective bulk permeability of the model domain is

$$k = -\frac{Q\mu L}{A(P_2 - P_1)}, \quad (8)$$

where Q is defined numerically by Eq.6; and A is the area of the flow domain in the horizontal, A_h , or vertical, A_v , direction.

The analytical calculations of permeability for Verification Test #2 are shown in Table 1. In Table 2, numerical and analytical results of effective permeability can be compared.

Volumetric porosity, n_v , of the domain is equal to the sum of the volumes of individual fractures divided by the volume of the domain:

$$n_v = (N_{\text{vertical}} * V_{\text{vertical}} * \phi_{f-v} + N_{\text{horizontal}} * V_{\text{horizontal}} * \phi_{f-h}) / V_{\text{domain}} \quad (9)$$

where V_{vertical} and $V_{\text{horizontal}}$ are the volumes of individual vertical and horizontal fractures, respectively, calculated as fracture area times fracture aperture, defined by Eq. 2; N_{vertical} and $N_{\text{horizontal}}$ are the numbers of vertical and horizontal fractures in the domain; ϕ_{f-v} and ϕ_{f-h} are the internal fracture porosities of the vertical and horizontal fractures, which can vary between 0 and 1 due to mineral infilling; and V_{domain} is the volume of the simulation domain, in this case $V_{\text{domain}}=10^6 \text{ m}^3$. Volumetric porosity is also known as the P_{33} DFN parameter, defined as the fracture volume per domain unit volume (Table 2).

Transport porosity n_t is calculated directly from the particle breakthrough curves, and reflects the combined effects of the volumetric porosity (including the internal fracture porosity), and the effects of flow channeling that can cause some of the volumetric porosity to be bypassed.

Transport porosity is calculated from the flux q and the mean particle breakthrough time t_{50} from which the mean transport velocity can be calculated as $v = L/t_{50}$. From the relationship $n_t = q/v$, we obtain

$$n_t = \frac{q t_{50}}{L}, \quad (10)$$

where q is a sum of input fluxes (Eq.5), t_{50} is the time at which the CDF of the BTC has a value of 0.5, and L is the length of the transport domain. Results of calculated transport porosities are shown in Table 2 for the two cases that assume different internal fracture porosities ($\phi_f = 0.25$ and $\phi_f = 1.0$), with t_{50} taken from the breakthrough curves in Fig. 7 for each case.

Table 2. Upscaled parameters for DFN verification test #2

	Effective bulk permeability obtained by numerical calculation (Eq.8) (m^2)	Effective bulk permeability estimated analytically using data in Table 1 ¹ (m^2)	Volumetric porosity, n_v (Eq.9) ($\phi_f=0.25$)	Volumetric porosity, n_v (Eq.9) ($\phi_f=1.0$)	Transport porosity n_t (Eq.10) ($\phi_f=0.25$)	Transport porosity n_t (Eq.10) ($\phi_f=1.0$)
Horizontal flow, east-west and south-north	2.44e-13	2.47e-13	1.807e-3	7.23e-3	1.09e-3 (E-W/W-E) 1.21e-3 (N-S/S-N)	4.32e-3 (E-W/W-E) 4.86e-3 (N-S/S-N)
Vertical flow direction, top-bottom	5.76e-14	5.08e-14	1.807e-3	7.23e-3	4.89e-4 (T-B/B-T)	2.07e-3 (T-B/B-T)

¹ The permeability in the horizontal direction was computed using only the properties of the horizontal fractures listed in Table 1, because the vertical fractures do not extend to the boundaries. The permeability in the vertical direction used only the properties of the vertical fractures in Table 1, because no horizontal fractures intersected the top or bottom boundaries.

It is interesting to note that even for this simple fracture system, the transport porosities are less than the volumetric porosity because not all of the porosity is accessed equally by the particles during transport. It is also interesting to note that transport porosity depends on flow direction, an aspect of fracture systems that is not often recognized. The calculated transport porosities for the horizontal (E-W/W-E and N-S/S-N) particle transport results and $\phi_f = 1.0$ are similar to the volumetric porosity of the horizontal fractures (5.22e-3 for $\phi_f = 1.0$) whereas the calculated transport porosity for the T-B/B-T transport results are more similar to the volumetric porosity of the vertical fractures (2.01e-3 for $\phi_f = 1.0$). The same relationships hold when $\phi_f = 0.25$. This reflects the fact that fractures perpendicular to the direction of flow do not fully participate in the transport process. It is also notable that the bulk permeability calculated from the modeled fluxes using equation (8) agrees well with the bulk permeability calculated from the fluxes calculated analytically for individual horizontal or vertical fractures in Table 1, indicating that the vertical fractures do not augment the overall permeability of the domain, even though they span 80 percent of the flow domain in the N-S direction.

4. Transport modeling in DFNs based on fracture characteristics of the Topopah Spring Aquifer and the Lava Flow Aquifer

In order to generate fracture networks similar to the Topopah Spring Aquifer (TSA) and Lava Flow Aquifer (LFA) at Pahute Mesa, we use fracture characteristic data obtained from Golder and Associates in [Tech. Mem., 2015; NSTec, 2014 (Appendix L)], which includes both field observations and modeling estimates.

Information on the following fracture characteristics is required to generate fracture networks: statistical parameters of fracture size distribution, statistical parameters of fracture orientation distribution, and fracture intensity. Data from Table 12 in [NSTec 2014 (Appendix L)] are used to represent fracture orientations for the TSA and LFA. Table 13 in [NSTec 2014 (Appendix L)] describes statistical parameters of fracture size distributions. Fracture intensity is calculated as $P_{32}=A \cdot \exp(-B \cdot \text{thickness})$, where coefficients A and B are given in Table 17 in [NSTec 2014 (Appendix L)]. Copies of Tables 12, 13, and 17 of NSTec 2014 (Appendix L) are included in the Appendix of this document so that the reader can refer to the fracture properties used in the analyses.

4.1 Challenges in DFN generation

Based on the fracture characteristics, fractures in the TSA and LFA are observed to be non-homogeneous and cannot be generated using the same method described above for the simple DFN examples.

The LFA and TSA are divided into cooling sub-units (CSU) or layers; the LFA has 4 CSUs and the TSA has 3 CSUs. Each layer consists of a mix of orthogonal cooling joints and tectonic fractures, which represent 5 different fracture sets [Tech. Mem., 2015; Appendix L, 2015]. For the FY2015 work, we used the *mathematica* modeling package to generate the corresponding fracture network. In this version of the fracture generation algorithm, each layer of fractures is produced independently. Afterward, the layers are combined together into an entire simulation domain. In this case, the computational cost is very high because *mathematica* does not allocate memory properly when working with large data sets and high fracture intensity, defined for TSA and LFA, is not generated in reasonable computational time. In order to reduce computational cost the following steps were performed:

- a) We increased the minimum cut-off for fracture length from 1 m to 5 m. This means that no fracture with a length less than 5 m was included in the DFNs. By this action, we assumed that small fractures do not have a significant effect on the overall flow and contaminant transport through the larger network. However, even with this larger minimum fracture size, the network was too large to generate with *mathematica* due to excessive run time and memory usage. Moreover, the desired fracture intensity was not achieved.
- b) The next step was to decrease the domain size to make the problem more tractable. The height of the domain was kept the same (100m) in order to maintain the thicknesses of the cooling subunits. The new domain size is 50m x 50m x 100m. In this case, we were able to generate DFNs with fracture intensity close to the desired value discussed above, using the 5-m minimum fracture length. The results shown below correspond to this reduced domain size.

In order to overcome the computational restrictions of high intensity DFN generation, the algorithms originally in the *mathematica* code were reproduced using the C++ programming platform. Preliminary results for the new version of fracture generation are shown in Section 5.

Figure 10 shows two DFN realizations of the LFA (top panels) and two DFN realizations of the TSA aquifer (bottom panels). By generating each layer independently, the required intensities P_{32} , given in [Tech. Mem., 2015; Appendix L, 2015] are achieved. During the process of combining layers together with tectonic fractures sets, the intensity tends to decrease due to rejection of overlapping fractures by the Feature Rejection Algorithm for Meshing, FRAM [Hyman et al., 2014].

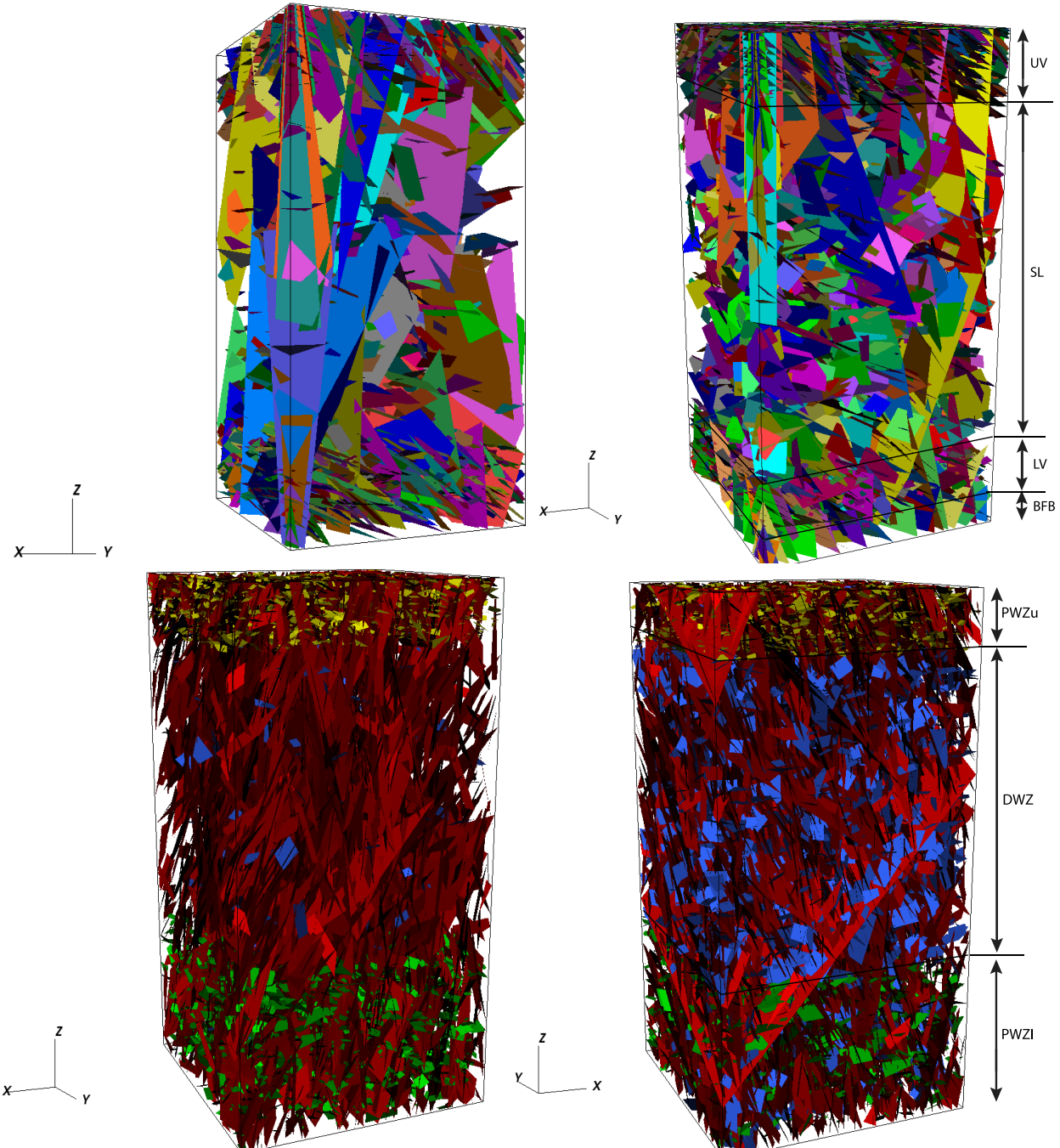


Figure 10. Two DFN realizations of the LFA (top panels) and two DFN realizations of the TSA (bottom panels) are shown. In the DFNs for the LFA, four CSUs are included and each fracture is represented by its own color. The DFNs of the TSA are colored by the three CSUs; red shows tectonic fracture sets, T1 and T2, which cross the entire TSA domain; yellow, blue and green indicate the cooling fracture sets in the three different layers.

4.2 Flow Solution and Transport Modeling in DFNs for the TSA and LFA

In this study, the PFLOTRAN [Lichtner et al., 2015], multiphysics code is used to obtain steady-state pressure solutions for fully saturated flow on the DFNs. PFLOTRAN is a high-performance computing (HPC) code that runs on multiprocessors and operates with large data sets. For example, the DFN realization of the TSA consists of 12,702 fractures, and the computational mesh has 6,463,596 control volume cells and 12,980,611 triangular elements.

Before the boundary conditions are applied to the domain sides, the transmissivity and aperture of fractures are defined as functions of fracture size using Eq. 1 and Eq.2, respectively. Figure 11 shows aperture and transmissivity values as functions of fracture lengths; the plots verify that the equations governing aperture and transmissivity are implemented correctly in the current simulations.

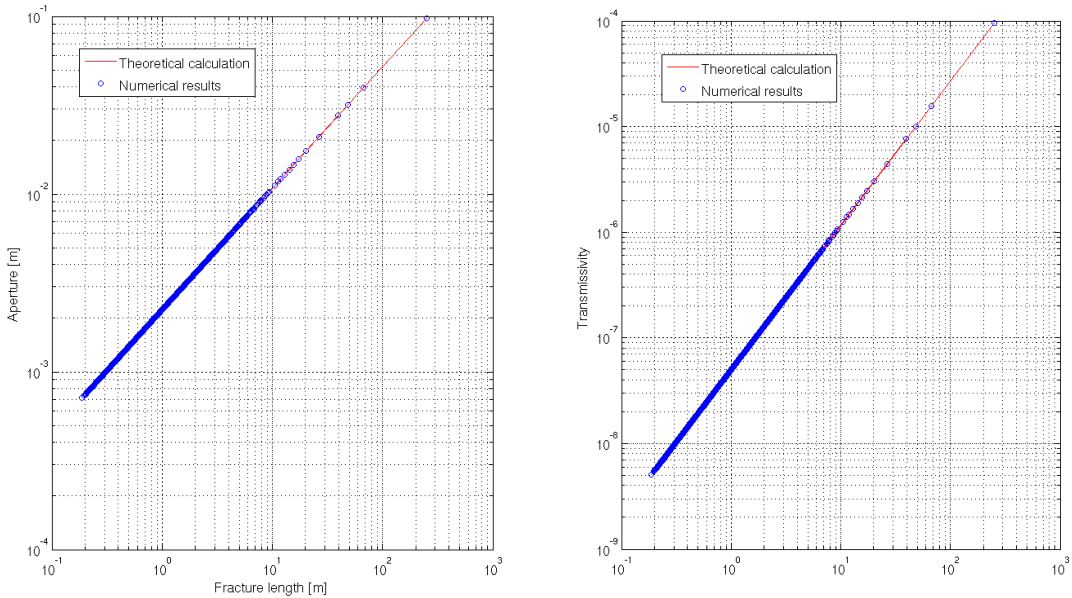


Figure 11. Theoretical calculation (Eqs. 1 & 2) and numerical results are compared for aperture (left panel) and transmissivity (right panel) versus fracture lengths for a DFN realization with TSA fracture characteristics.

The applied pressure gradient is defined by Eq. 3. Pressure boundary conditions are applied to opposite sides of the domain to represent in-flow and out-flow boundaries; no-flow boundaries are used on the other domain boundaries. Examples of horizontal flow solutions, both west to east and north to south, are shown in Figures 12 and 13 for DFNs of the LFA and TSA, respectively.

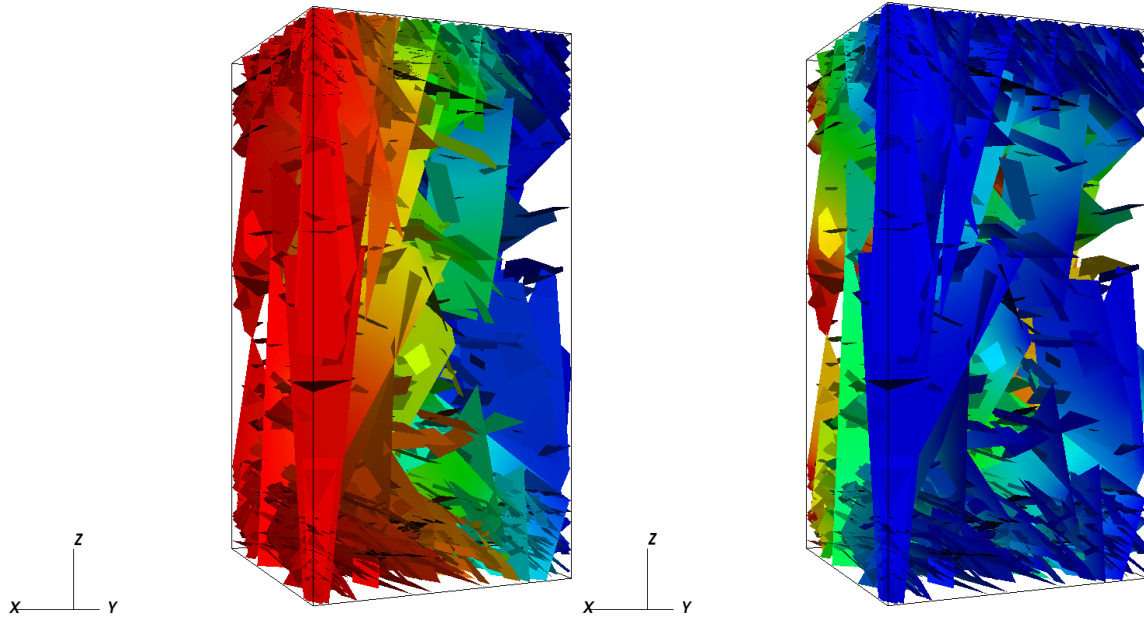


Figure 12. Pressure solutions for fully saturated flow obtained for DFN realizations with LFA fracture characteristics. Blue colors represent low pressure and red colors are high pressures along the in-flow boundaries. The left panel is for a case with flow along the x axis, from west to east. The right panel is for a case with flow along the y axis, from north to south.

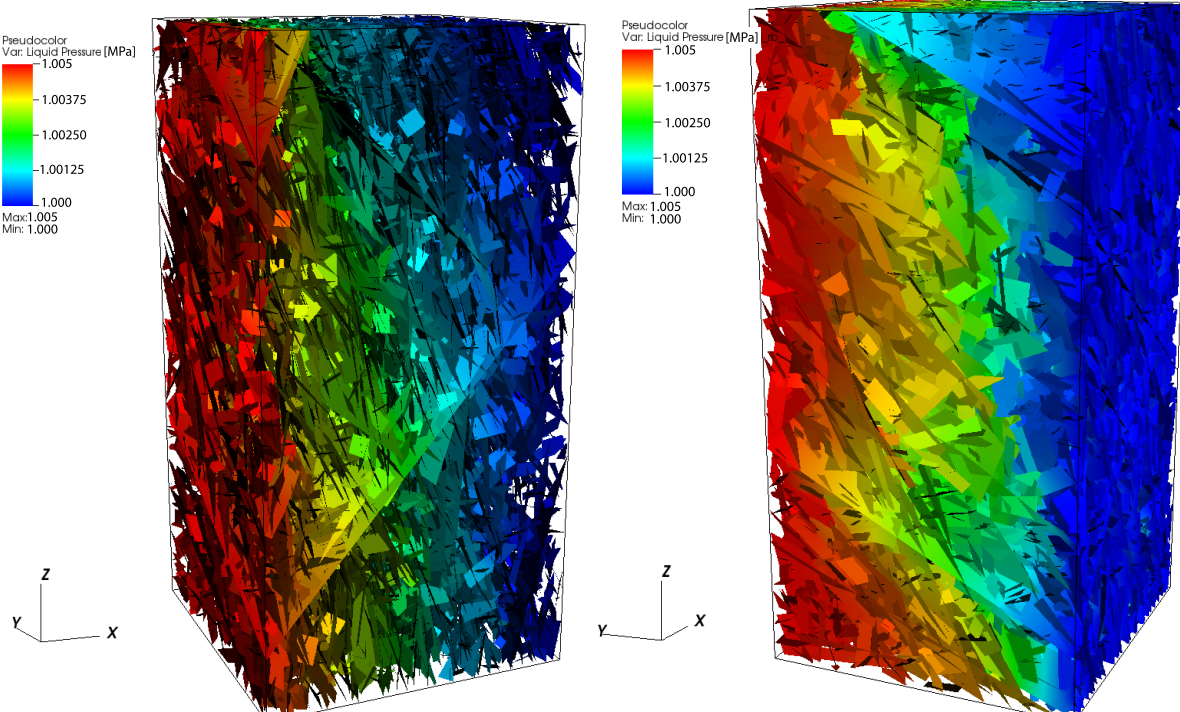


Figure 13. Pressure solutions for fully saturated flow obtained for DFN realizations with TSA fracture characteristics. Blue colors represent low pressure and red colors are high pressure, the pressure gradient is along the flow direction. The left panel is for a case with flow along the x axis, from west to east. The right panel is for a case with flow along the y axis, from north to south.

Figures 14 and 15 show particle trajectories moving from north to south in DFNs for the LFA and TSA, respectively. We use the particle tracking approach described in [Makedonska et al., 2015] to model advective transport in three-dimensional DFNs. In the considered simulation set, all particles initially are placed equidistant on each fracture edge along the in-flow boundary, regardless of fracture size. As particles move through the DFN and meet fracture intersections, they tend to continue travelling through the large fractures, which have higher transmissivity. As a result, channeling of particles through larger fractures is observed. However, there is a non-zero probability for particles to move through small fractures, which makes their travel time longer. These particles contribute to the tails of travel time distributions. Because the fracture intensity is different in each CSU, the initial particle distribution is not equal along the in-flow boundary. The unit with the highest fracture intensity has a larger number of fractures on the in-flow boundary and, as a result, a larger number of particles were placed initially at that layer. Also, larger instantaneous velocities are correlated to longer aperture, which can be visually seen in Figures 14 and 15 bottom panels.

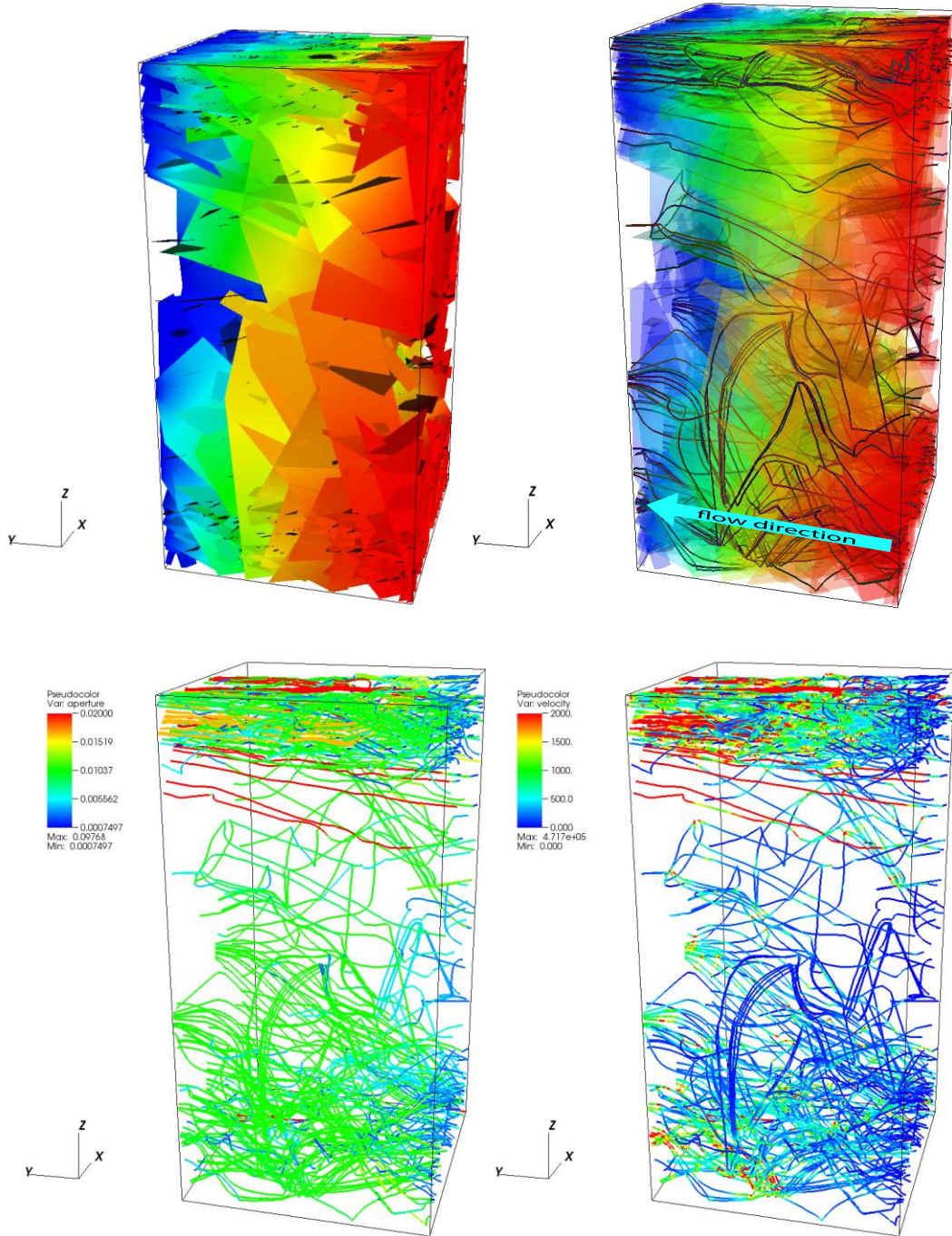


Figure 14. Pressure solutions and particle trajectories are shown for DFN realizations with LFA fracture characteristics. This case shows transport along the y axis, from north ($-y$) to south ($+y$). The upper panels show the flow solution, and the upper right panel includes particle trajectories moving from north ($-y$, right) to south ($+y$, left). The same particle trajectories are shown in the bottom panels, colored by fracture aperture [m] (bottom left) and particle instantaneous velocity [m/year] (bottom right).

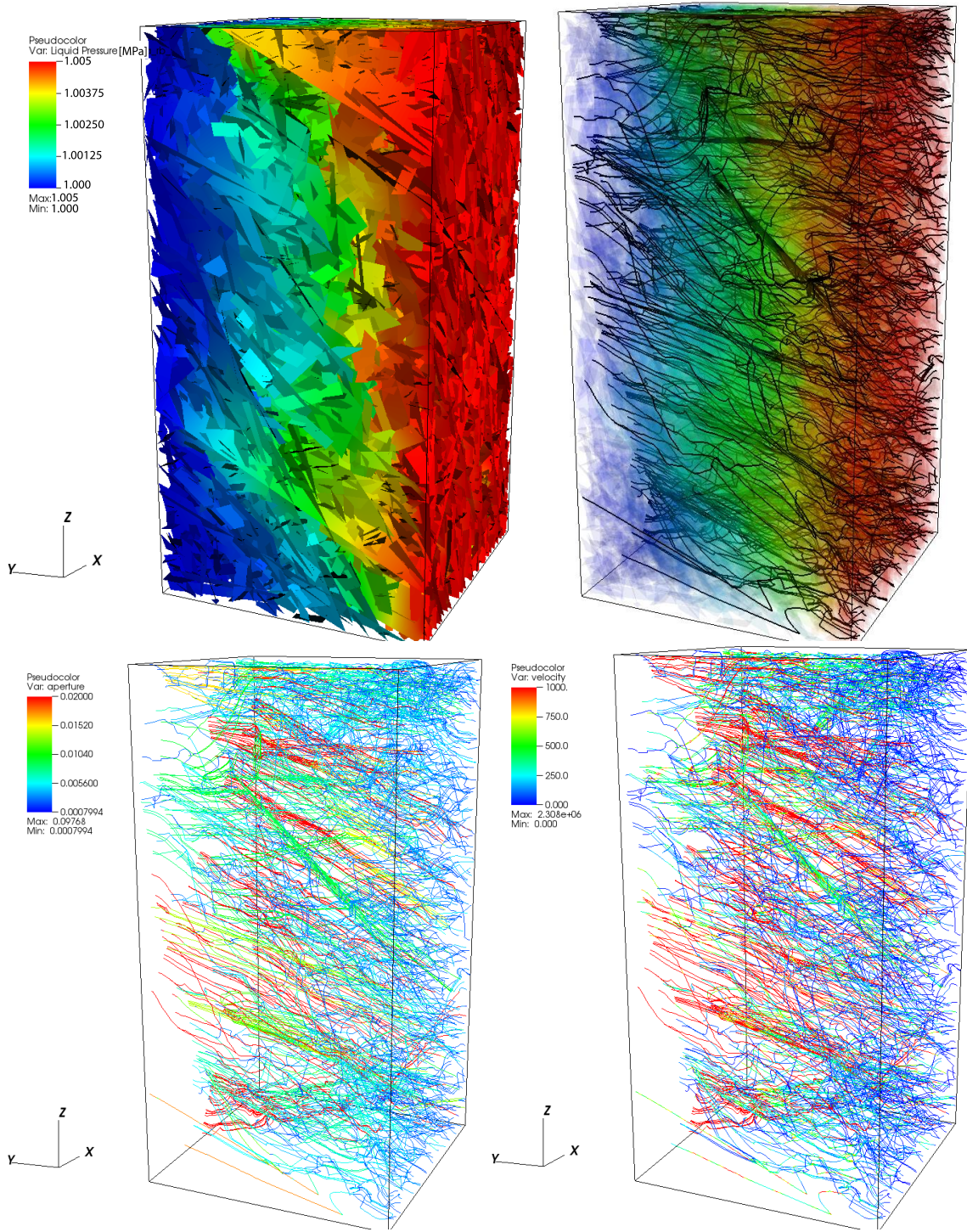


Figure 15. Pressure solution and particle trajectories are shown for a DFN realization with TSA fracture characteristics. This case shows transport along y axis, from north ($-y$) to south ($+y$). The upper panels show the pressure flow solution. The upper right panel shows particle trajectories moving from north ($-y$) to south ($+y$) direction. The same trajectories are shown in the bottom panels, colored by fracture aperture [m] (bottom left) and particles instantaneous velocity [m/year] (bottom right).

Figure 16 shows BTCs of 150,000 particles simulated in each direction of flow for two independent DFN realizations for both the TSA and LFA. The averaged results are shown for transport in the LFA (left panel) and the TSA (right panel). For simulations of the TSA, we observe better agreement between travel time statistics in different directions of transport on earlier times. Statistics of later times shows more divergence in both aquifer models, TSA and LFA. Here, the internal fracture porosity is 0.25.

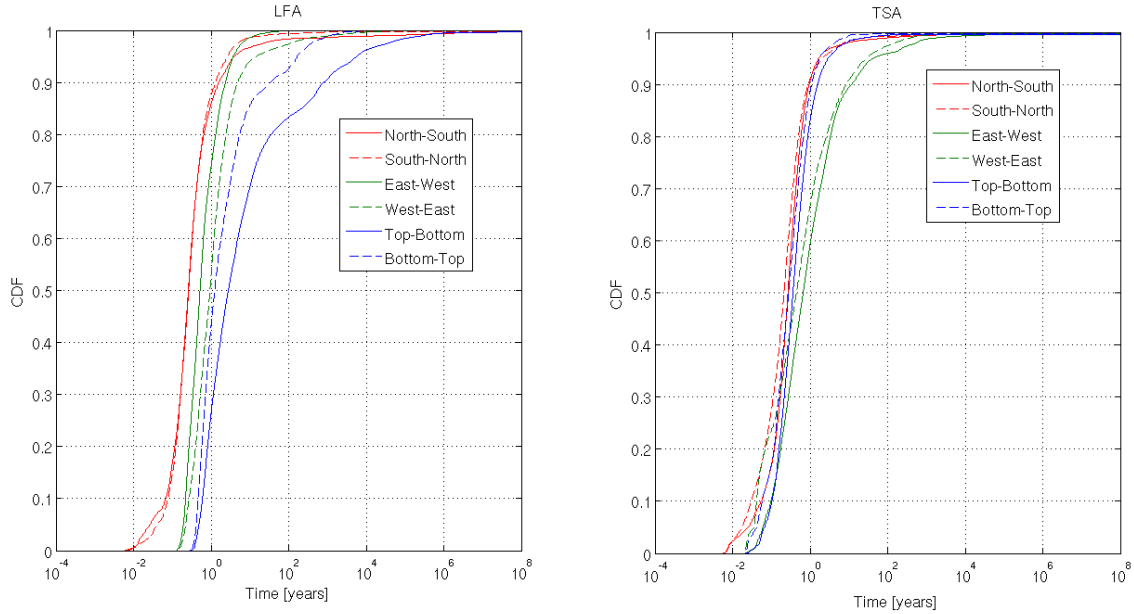


Figure 16. BTCs of transport in DFNs for the LFA (left panel) and the TSA (right panel).

Effective permeability, k [m^2], of the DFNs is calculated by Eq. 8. Estimated effective permeability, volumetric porosity and transport porosity are shown in Table 3. The significant anisotropy of effective permeability in north-south and east-west directions (approximately an order of magnitude) is observed for both the TSA and LFA because fracture orientations are dominantly north-south. Here transport porosity, calculated by Eq.10, is more than an order of magnitude smaller than volumetric porosity due to preferential flow through high transmissivity fractures, which causes flow channeling. For comparison, Navarro (2015) used a mean permeability of $k=4.86 \times 10^{-14} \text{ m}^2$ and a range of $4.86 \times 10^{-16} \text{ m}^2$ to $4.86 \times 10^{-12} \text{ m}^2$ for the TSA and a mean of $k=1.49 \times 10^{-12} \text{ m}^2$ and a range of $2.36 \times 10^{-14} \text{ m}^2$ to $9.41 \times 10^{-11} \text{ m}^2$ for the LFA in the statistical uncertainty analysis of the ER-20-11 multi-well aquifer test. The calculated, upscaled permeabilities of the TSA and LFA are in the range of likely values estimated from single-well and cross-well pump test data.

Table 3. Upscaled parameters for the TSA and LFA

Effective permeability, k (m^2)			
	North-South/South-North	East-West/West-East	Top-Bottom/Bottom-Top
TSA	6.05×10^{-13}	5.23×10^{-14}	1.86×10^{-14}
LFA	3.42×10^{-11}	2.39×10^{-12}	9.77×10^{-14}
Transport porosity ¹ (dimensionless)			
	North-South/South-North	East-West/West-East	Top-Bottom/Bottom-Top
TSA	4.187×10^{-4}	2.837×10^{-5}	3.856×10^{-4}
LFA	1.945×10^{-4}	2.008×10^{-5}	2.3405×10^{-4}
Volumetric porosity ¹ (dimensionless)			
TSA	7.1×10^{-3}		
LFA	3.9×10^{-3}		

¹Volumetric and transport porosity reflect an internal fracture porosity of $\phi_f = 0.25$, which is assumed to reflect mineral infilling.

5. Future Work on Improving Modeling Tools for Contaminant Transport Simulation

There are several steps that should be performed to increase software effectiveness and accuracy. These steps will be followed by incorporating results of advective transport into the modeling tool *MARFA* to evaluate the effect of sorption and matrix diffusion on radionuclide transport.

Currently, the fracture generation algorithm is being converted into C++ programming language, which allows reasonable memory usage with reasonable run times during generation of DFNs with high fracture intensity. Figure 17 shows preliminary results of a DFN generated with the C++ code, using TSA fracture characteristics. The size of the simulation domain is 100m x 100m x 100m. The entire DFN consists of 33,405 fractures, and represents three layers: the lower layer (PWZ1) - 100m x 100m x 30m, the middle layer (DWZ) - 100m x 100m x 60m, and the top layer (PWZu) - 100m x 100m x 10m. Here all layers are generated simultaneously, while the previous version generated using the *mathematica* code required each layer to be generated independently and required an additional step of combining all the layers into one fracture network. The entire mesh of the DFN shown in Figure 17 consists of 49,342,229 control volume cells. The new code is very effective in CPU computational time: for comparison, the DFN shown in Figure 17 is generated in 2.1 minutes of CPU time, while the *mathematica* code took 5-7 days to generate a final version of one DFN realization. As of the end of FY15, the new DFN generation tool is going through final testing. The next step is to incorporate the fracture generation code into the entire DFNWorks workflow illustrated in Figure 1. The new ability to model larger simulation domains (i.e., 100m x 100m x 100m, 200m x 200m x 100m) will allow us to compare BTCs with those obtained for the smaller domains presented in the current report.

The scale of groundwater flow and transport modeling can have a significant effect on radionuclide transport results. We are working on developing scale-dependent matrix diffusion and sorption models to integrate observations of sorption coefficients across scales. In order to evaluate the effect of sorption and matrix diffusion on radionuclide transport through fractured domains, we will incorporate pathlines of simulated advective transport into MARFA as a postprocessing step. MARFA simulates the effects of matrix diffusion and fracture or matrix sorption on particle breakthrough through the DFN, thereby providing a basis for estimating the effective matrix block sizes, effective

aperture, and effective upscaled sorption coefficients by fitting simpler algorithms to the modified breakthrough curves.

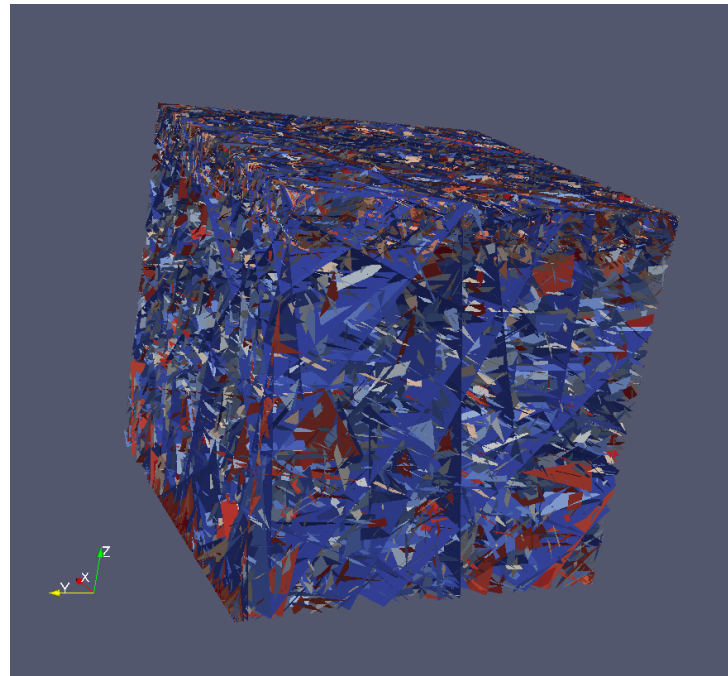


Figure 17. DFN realization of the TSA aquifer, produced using a new DFN generator (C++ code), which allows for generation of high intensity DFNs.

References

Coxeter, H.S.M. (1969). *Introduction to geometry*. John Wiley and Sons, 216–221.

Hyman J. D., Gable C. W., Painter S. L., and Makedonska N. (2014). Conforming Delaunay triangulation of stochastically generated three dimensional discrete fracture networks: A feature rejection algorithm for meshing strategy, *SIAM Journal of Scientific Computing*, 36(4), A1871–A1894.

Hyman, J. D., Karra, S., Makedonska, N., Gable, C. W., Painter, S. L., & Viswanathan, H. S. (2015a). *dfnWorks*: A discrete fracture network framework for modeling subsurface flow and transport. *Computers & Geosciences*, 84, 10-19.

Hyman J. D., Painter S. L., Viswanathan, H. S., Makedonska, N., and Karra, S. (2015b). Influence of Injection Mode on Transport Properties in Kilometer-Scale Three-Dimensional Discrete Fracture Networks, *Water Resources Research*, DOI: 10.1002/2015WR017151.

LaGrIT (2013) *Los Alamos Grid Toolbox*, (LaGrIT), <http://lagrit.lanl.gov>, Los Alamos National Laboratory.

Lichtner P. C., Hammond G. E., Lu C., Karra S., Bisht G., Andre B., Mills R. T., and Kumar J. (2015). *PFLOTRAN user manual: A massively parallel reactive flow and transport model for describing surface and subsurface processes*, Technical report, Los Alamos National Laboratory.

Makedonska N., Painter S. L., Bui Q. M., Gable C. W., and Karra S. (2015). Particle tracking approach for transport in three-dimensional discrete fracture networks, *Computational Geosciences*, DOI: 10.1007/s10596-015-9525-4.

Makedonska N., Painter S. L., Hyman J.D., Karra S., Gable C. W., and Viswanathan H.S. (2015). Evaluating the Effect of Internal Aperture Variability on Tracer Transport in Large Discrete Fracture Networks, *in preparation*.

Navarro, 2015. Pahute Mesa well development and testing analysis for well ER-20-11, Nevada National Security Site, Nye County, Nevada. N/0002653—xxx. Las Vegas, NV.

Painter S., Cvetkovic V., Mancillas J., Pensado O. (2008). Time domain particle tracking methods for simulating transport with retention and first-order transformation, *Water Resour. Res.*, 44.

Painter S., Gable C., Kelkar S. (2012). Pathline tracing on fully unstructured control-volume grids, *Comput. Geosci.*, 16, pp. 1125–1134

Painter, S., Mancillas, J., (2013). MARFA User's Manual: Migration Analysis of Radionuclides in the Far Field. *Posiva Working Report 2013-01*, Posiva Oy, Helsinki Finland

NSTec (draft November 2014). Phase II Hydrostratigraphic Framework Model for Corrective Action Units 101 and 102: Central and Western Pahute Mesa, Nye County, Nevada, DOE/NV/25946-xxx.

SKB (2011), Long-term safety for the final repository for spent nuclear fuel at Forsmark, SKB TR-11-01. Swedish Nuclear Fuel and Waste Management Co., Stockholm.

Technical Memorandum (2015), Golder Associates, Summary of Conceptual Model For Fractures in Lava Flow Aquifers at Pahute Mesa. Summary of Conceptual Model For Fractures in Topopah Spring Aquifers at Pahute Mesa.

Appendix:

The fracture characteristics data used for DFN generation of TSA and LFA aquifers [NSTec 2014 (Appendix L)].

Table 12: Orientation set probability model for cooling joints and tectonic fractures at Pahute Mesa by HSU

HSU ID	CSU ID	Fracture Set	Probability Distribution	Mean Pole (°)		Major Axis (°)		Fisher Concentration	
				Trend	Plunge	Trend	Plunge	K / K1	K2
LFA	All	SP	Univariate Fisher	89.12	27.35	n/a	n/a	18.34	n/a
LFA	All	DP	Univariate Fisher	350.48	28.06	n/a	n/a	26.24	n/a
LFA	All	BP	Univariate Fisher	19.39	53.21	n/a	n/a	35	n/a
LFA	All	T1	Univariate Fisher	319.06	18.73	n/a	n/a	35	n/a
LFA	All	T2	Univariate Fisher	48.39	7.85	n/a	n/a	35	n/a
TCA	All	CJ1	Elliptical Fisher	267.64	7.07	43.47	80.24	9.56	3.56
TCA	LHFL, SFCL	CJ2	Elliptical Fisher	179.28	19.79	359.6	70.21	8.15	1.83
TCA	All	CJ3	Elliptical Fisher	352.99	76.86	181.68	12.99	14.06	1.82
TCA	All	T1	Elliptical Fisher	125.66	4.88	340.06	84.09	9.06	3.63
TCA	All	T2	Univariate Fisher	44.61	12.2	n/a	n/a	9.82	n/a
TSA	All	CJ1	Elliptical Fisher	95.78	9.14	235.27	78.05	10.33	2.09
TSA	All	CJ2	Elliptical Fisher	1.58	4.71	179.58	85.29	10.52	5.28
TSA	All	CJ3	Elliptical Fisher	5.68	79.4	138.61	7.27	10.15	2.48
TSA	All	T1	Elliptical Fisher	134.72	12.51	340.41	76.16	12.99	1.82
TSA	All	T2	Elliptical Fisher	44.09	17.6	192.33	69.55	10.41	4.46

Table 13: Size model for cooling joints and tectonic fractures at Pahute Mesa

HSU ID	CSU ID	Fracture Set	Probability Distribution	Parameter Names	Distribution Parameters	Size Truncation	Aspect Ratio
LFA	All	SP	Unit Thickness		n/a	n/a	5
LFA	All	DP	Unit Thickness		n/a	n/a	5
LFA	All	BP	Exponential	Mean	3.373	Min = 1m	1
LFA	All	T1	Power Law	k_r, r_0	2.6, 1	Min = 1m, Max = 250m	5
LFA	All	T2	Power Law	k_r, r_0	2.01, 1	Min = 1m, Max = 250m	5
TSA	All	CJ1	Unit Thickness		n/a	n/a	5
TSA	All	CJ2	Unit Thickness		n/a	n/a	5
TSA	All	CJ3	Exponential	Mean	3.373	Min = 1m	1
TSA	All	T1	Power Law	k_r, r_0	2.6, 1	Min = 1m, Max = 250m	5
TSA	All	T2	Power Law	k_r, r_0	2.01, 1	Min = 1m, Max = 250m	5

Table 17: Fracture intensity models as a function of HSU and CSU for Pahute Mesa

HSU	CSU	Set	Probability Model	A	B
LFA	UV	All	Exponential	1.462	0.063
LFA	SL	All	Exponential	0.985	0.035
LFA	LV	All	Exponential	0.500	0.033
LFA	BFB	All	Exponential	0.003	0.704
TSA	PWZu	CJ1	Exponential	5.000	0.150
TSA	PWZu	CJ2	Use CJ1 Fit		
TSA	PWZu	CJ3	Use CJ3 from PWZI fit		
TSA	PWZu	T1	Use T1 from PWZI fit		
TSA	PWZu	T2	Exponential	0.300	0.050
TSA	DWZ	CJ1	Exponential	0.080	0.022
TSA	DWZ	CJ2	Exponential	1.000	0.060
TSA	DWZ	CJ3	Exponential	0.500	0.035
TSA	DWZ	T1	Exponential	1.000	0.025
TSA	DWZ	T2	Exponential	0.009	0.021
TSA	PWZI	CJ1	Exponential	3.000	0.050
TSA	PWZI	CJ2	Exponential	1.000	0.070
TSA	PWZI	CJ3	Exponential	0.500	0.050
TSA	PWZI	T1	Exponential	0.500	0.050
TSA	PWZI	T2	Exponential	0.400	0.380